



Optimizing the Performance of the Meso-Scale Continuous-Flow Photoreactor for Efficient Photocatalytic CO₂ Reduction with Water Over Pt/TiO₂/RGO Composites

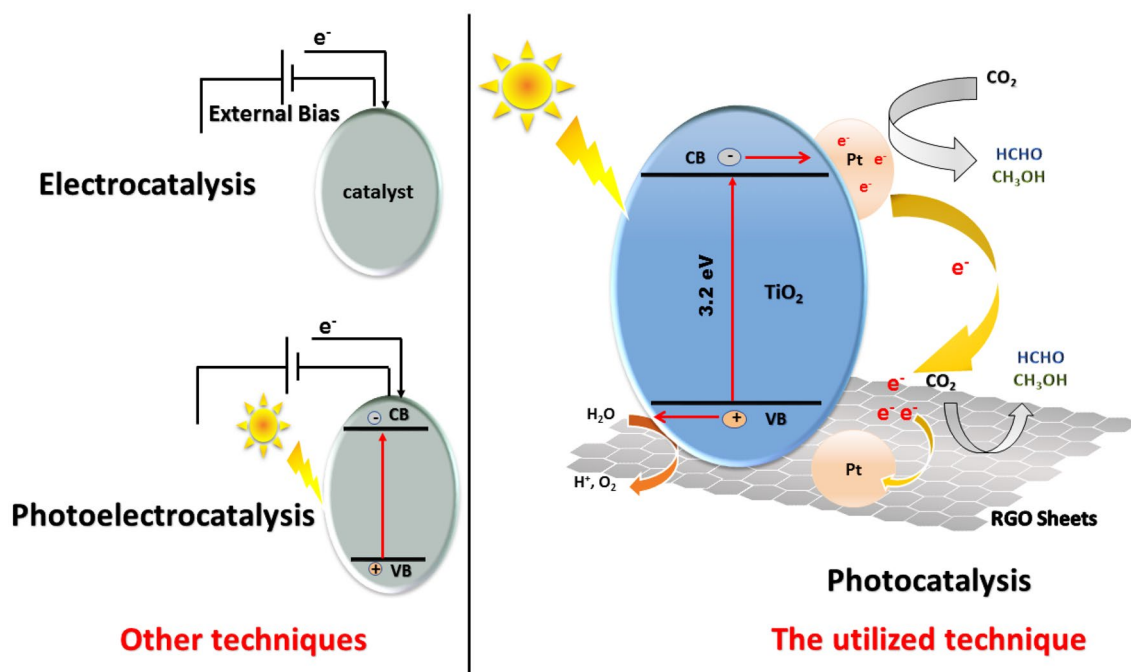
Samar Nabil¹ · Elsayed A. Shalaby¹ · Marwa F. Elkady^{2,3} · Yoshihisa Matsushita⁴ · Ahmed H. El-Shazly^{2,5}

Received: 21 October 2021 / Accepted: 30 December 2021 / Published online: 22 January 2022
© The Author(s) 2022

Abstract

Tuning the reaction parameters to maximize products yield is one of the major needs for any process. The goal of this research is to increase the reduction of CO₂ with water by examining the operating parameters of a meso-scale continuous-flow type photochemical reactor over hydrothermally synthesized photocatalysts such as Pt/TiO₂ and Pt/TiO₂/RGO. Effects of catalyst type, weight of catalyst utilized, photochemical reactor temperature, retention time by varying the liquid water flow rate, and cocatalyst loading were investigated to increase the concentration of total organic carbon compounds including HCHO and CH₃OH. The effect of titanium dioxide phase ratio (anatase: rutile) presence at the Pt/TiO₂/RGO photocatalysts was also studied. The results revealed that the 0.3 wt.% Pt/TiO₂/RGO_{5%} photocatalyst which includes a phase ratio of 81:19 for anatase: rutile respectively has the superior photocatalytic activity to other studied photocatalysts. The physicochemical properties of different prepared photocatalytic samples were determined using various characterization techniques. Analyzing the liquid products on gas chromatography, it was found that CH₃OH represents the major product whereas HCHO was the minor one. This reactor exhibits a great performance towards CO₂ photocatalytic reduction under the optimized conditions.

Graphical Abstract



Keywords CO₂ photocatalytic reduction · Pt/TiO₂/RGO · Continuous flow reactors · (Anatase: rutile) ratio

1 Introduction

The global warming effect is the most serious environmental problem confronting humanity. One of the greenhouse gases (GHG) that contributes to climate change is carbon dioxide (CO₂). The earth's temperature increases as a result of infrared light absorption by CO₂ and other GHG then re-emitting this radiation to the surface of earth leading to the global warming effect [1, 2].

However, most of the emitted CO₂ occurs from the combustion of fossil fuel which facing a depletion risk. Thus, the photoconversion of CO₂ which is a mimic of the plant photosynthesis was a reasonable solution to turn CO₂ in the existence of water and solar energy into hydrocarbon fuels. This method considers a very promising method not only to eliminate CO₂ emissions but also to produce useful hydrocarbons such as formic acid (HCOOH), formaldehyde (HCHO), methanol (CH₃OH), methane (CH₄) and ethanol (C₂H₅OH), etc. [2].

The photo-conversion of CO₂ has many limitations which control the conversion efficiency and the yield of products. Some of those limitations are related to the semiconductor utilized and others are directly related to the design of the used reactor.

Titanium dioxide (TiO₂) is a common semiconductor applied in the CO₂ photoreduction due to its corrosion resistance, long-term stability, nontoxicity and low cost [3, 4]. However, it has many disadvantages not only the recombination of electron–hole pairs but also it needs UV irradiation to activate. Thus, many trials had been performed to overcome those limitations by noble metals loading and the usage of carbonaceous nanomaterials such as carbon nanotube, carbon nanowalls, and graphene [5]. Among the carbonaceous nanomaterials, graphene based photocatalysts have found to improve the visible light absorbance which consequently enhances the rate of CO₂ reduction [3, 6].

Many previous studies examined the usage of noble metals such as (Au, Rh, Ag, Pt) and their loading amounts on TiO₂ photocatalyst. They confirmed that the most effective one among those metals was Pt.

Xie et al. [7] investigated the effect of different noble metals loading on the TiO₂ and found that the CH₄ formation rate enhanced with the following order Pt > Pd > Au > Rh > Ag. Also, Li et al. [8] studied the effectiveness of noble metals loading on the photoreduction of CO₂ and found that efficiency followed the sequence of Pt > Au > Ag.

In addition, many trials were conducted to enhance the yield of products from CO₂ photoreduction especially using continuous mode reactors. The use of water vapor with CO₂ gas was commonly utilized to form a single phase of

reactants therefore increasing of products yield. Sim et al. [9] examined the use of water vapor and the ternary composite of reduced graphene oxide/Pt–TiO₂ nanotube arrays in a gas–solid photoreactor to produce CH₄ after the photocatalytic reduction of CO₂. Moreover, Tan et al. [10] studied the photoreduction of CO₂ using various noble metals anchored on reduced graphene oxide/TiO₂, however; the most efficient one was Pt which has further been used to form CH₄ via a continuous gas flow reactor.

Wang et al. [11] tested the usage of compressed CO₂ with water vapor in a continuous flow film reactor then the effluent gas was recorded in relation to the irradiation time duration. The results revealed that the CH₄ rates were dropped after 5 h of irradiation, and they attributed that to the decline of adsorption power of the used catalyst.

Kometani et al. [12] examined the photoreduction of CO₂ with H₂O over Pt loaded TiO₂ in a flow type reactor as a function of temperature and pressure up to 400 °C and 30 MPa. They proposed using liquified CO₂ to create such homogenous single-phase reactants, and they discovered that increasing the temperature from 300 °C to 400 °C at a constant pressure of 30 MPa enhanced the yields of CO, CH₄, HCOOH, and HCHO.

The use of high temperature and pressure to form single-phase reactants is economically unfavorable. Moreover, there are few reports discussed the photoreduction of CO₂ in continuous mode reactors especially with suspension photocatalyst.

In a prior work, our group introduced the utilization of an advanced meso-scale continuous-flow photochemical reactor to reduce CO₂ with liquid water. [13]. Findings revealed that the use of this reactor resulted in an outstanding performance for CO₂ photoreduction where its selectivity was focused toward methanol production and suppressing water reduction into H₂. Therefore, this study aims to optimize the operating conditions of the previously mentioned photochemical reactor with a reduced graphene oxide supported on a low platinum content (0.3 wt.%) over the TiO₂ semiconductor. Moreover, the effect of photocatalyst type, co-catalyst loading as well as (anatase: rutile) ratio were investigated in this work to improve the concentration of the total organic carbon (TOC) by comparing between the pre-synthesized binary and ternary composites (PTG1 and PTG2).

The performance of CO₂ photoreduction has been studied in relation to the following parameters: (1) the catalyst type including the effect of (anatase: rutile) ratio, (2) the weight of catalyst utilized, (3) the photochemical reactor temperature, (4) the liquid water flow rate, and (5) the cocatalyst loading.

2 Experimental

2.1 Materials

TiO₂ was bought from two different suppliers one from (ACROS) organics and the other one from Sigma-Aldrich. The two kinds of TiO₂ are differ than each other in (anatase: rutile) ratio. In order to distinguish between the two kinds of TiO₂, it will be referred to them as a T1 and a T2. (ACROS) organics provided the metal precursor of platinum salt (H₂PtCl₆.H₂O), while Fisher Scientific provided graphite powder and sodium sulphate (Na₂SO₄). All other chemicals were analytical grade and commercially available, such as iodine (99.99%) and potassium permanganate (KMnO₄).

Merck, Germany supplied the nitric acid (HNO₃). Sigma-Aldrich provided the hydrochloric acid (HCl), hydrogen peroxide (H₂O₂), and sulphuric acid (H₂SO₄), while Fisher Scientific provided the acetone (C₃H₆O) and ethanol (C₂H₅OH). All solvents were of the (HPLC) grade.

2.2 Samples preparation

After graphite oxide synthesis by the modified Hummers method, ternary composites of 0.3 wt.% Pt/TiO₂/RGO (PTG) with both forms of TiO₂ were synthesized in a one-step procedure utilizing the hydrothermal method [14].

Briefly, strong acids such as nitric acid (HNO₃) were used to convert graphite powder to graphite oxide, followed by the slow addition of sulphuric acid (H₂SO₄) in a vessel immersed in an ice bath under stirring and sonication, and then potassium permanganate (KMnO₄) was progressively added. To avoid temperature increases during the exothermic reaction, the temperature was kept below 20 °C using an ice bath, and the mixture was then allowed for 24 h with continuous stirring to finalize the oxidation process. Hydrogen peroxide was added to quench the reaction until a yellow–brown cake of graphite oxide (GO) was produced, which was then washed with HCl and distilled water multiple times by decantation.

Exfoliating the GO with distilled water was the first step in creating the ternary composite. Then, under sonication and vigorous stirring, both TiO₂ suspended in ethanol solution and metal precursor of platinum salt (H₂PtCl₆.H₂O) were blended with the GO solution. Finally, the mixture was placed in a Teflon-lined autoclave and held at 200 °C for 12 h. The powder was then cleaned and dried in a drying oven at 80 °C for 24 h.

2.3 Characterization of the as-prepared photocatalysts

The properties of the nanocomposites synthesized to be further used as photocatalysts in carbon dioxide reduction were studied by different techniques such as Transmission

Electron Microscopy (TEM), the high-angle annular dark-field scanning transmission electron microscopy (HAADF-STEM), Energy-Dispersive X-ray Spectroscopy (EDX), X-ray Diffraction Spectroscopy (XRD), Fourier Transform Infrared Spectroscopy (FTIR), Brunauer–Emmett–Teller (BET), UV–Vis diffuse reflectance spectroscopy (DRS), and photoelectrochemical (PEC) measurements.

The field-emission transmission electron microscope (FE-TEM) (JEOL JEM-2100F) was also used in order to identify the shape, distribution, size, and surface morphology of the photocatalysts.

The high-angle annular dark-field scanning transmission electron microscopy (HAADF-STEM) was done on a (JEOL JEM-2100F) TEM/STEM with a spherical aberration corrector.

In order to study the elemental analysis and the weight percentage of the samples, EDX was performed using energy-dispersive X-ray spectroscopy (JEOL JEM-2100F).

The phase and crystalline composition of the synthesized photocatalysts were studied by XRD pattern. Before the analysis, the samples were firstly milled into very fine powder. A 2theta scan ranging from 5° to 80° at a scanning pitch of 0.02° was performed using an X-ray diffractor (XRD-6100 Shimadzu, Japan) coupled with a Cu-Kα radiation source with a wavelength of 1.55 Å.

The functional groups contained in each photocatalyst were determined and specified using Fourier Transform Infrared Spectroscopy (FTIR). The FTIR spectrometer concurrently captures high-spectral-resolution data over a wide spectral range and analyses it, based on the infrared spectrum of absorption or emission of the materials. The spectrometer used was Vertex 70 IR (Bruker Scientific Instruments, Germany).

To investigate the specific surface area and pore size distribution, the Brunauer–Emmett–Teller (BET) method was used. The N₂ adsorption/desorption isotherms were investigated for the as-prepared photocatalysts. The photocatalysts' Brunauer–Emmett–Teller (BET) specific surface areas were measured at 77 K using a Belsorp-mini II (BEL JAPAN) nitrogen adsorption equipment. Prior to surface area analysis, the powders were degassed at 300 °C for 3 h under vacuum.

UV–vis spectrometer (JASCO V-630) with an integrating sphere was used to measure diffuse reflectance spectra. The band gap was calculated using the Kubelka–Munk function and reflectance data.

In the presence of 0.1 M Na₂SO₄ electrolyte, photoelectrochemical (PEC) measurements were performed using a potentiostat (Gamry instrument, reference 3000) in one compartment cell with a Pyrex window. The platinum rod and saturated Ag/AgCl were employed as counter electrode (C.E) and reference electrode (R.E), respectively, in a three-electrode setup while the working electrode (W.E.)

was made from various photocatalysts powder using electrophoretic deposition method (EPD) on the fluorine-doped tin oxide (FTO) glass surface. The light irradiation source was a UV LED lamp from (Suruga Seiki-Co, Japan) with a wavelength of 365 nm and an intensity of up to 50 mW/cm². After deposition of numerous catalysts on the surface of FTO glass, the weight and coated area of each working electrode were approximately 4 mg and 6 cm², respectively.

2.4 Photocatalytic reduction of CO₂ with H₂O

The photoreduction of CO₂ with water was conducted in a continuous-flow photochemical reactor system (Vapourtec UV-150) under inner UV light irradiation, as indicated in Fig. 1. The used reactor was constructed from channels with 1.3 mm inner diameter are made of thin-walled Fluorinated Ethylene Propylene (FEP) tubing which allow the penetration of light and its volume is equal to 10 ml. In order to save energy, the light source was a UV (LED) lamp with $\lambda = 365$ nm. The used reactor provides many advantages as the uniform inner irradiation, high surface area to volume ratio which improves photon and mass transfer also it could be operated with heating or cooling modes.

Different types and amounts of catalyst powders were dispersed first in 65 ml deionized water by using ultrasonication. Prior to illumination and to ensure complete saturation, pure CO₂ was bubbled at an average flow rate of 35 ml min⁻¹

for 30 min through the dispersed catalyst under a controlled chilled water bath to enhance the solubility of CO₂ in the mixture. After the flow was stabilized, the photochemical reactor started on and the pump feeds the suspension into the photochemical reactor with the desired flow rate, the UV LED lamp was turned on to commence the experiment.

Helium (He) was utilized as a carrier gas with a constant flow rate of 20 ml min⁻¹ to separate the produced gases into a gas bag purchased from (GL Sciences Inc., Japan) for the offline analysis. Then, it was analyzed by a GC (Shimadzu 2014, Japan) coupled with ShinCarbon ST micropacked column (Restek, length 2 m × ID 2 mm, U.S.A) and a thermal conductivity detector (TCD). After the analysis of the gas bag, neither CO nor CH₄ were detected. Also, the GC did not identify hydrogen gas (H₂), indicating that its amount was too little to be identified or that it was probably reacted.

In addition to that the cold trap was used to ensure that all organic vapors produced were condensed in the liquid phase. After filtering and extraction, the liquid products were evaluated qualitatively using GC/flame ionization detector (FID) (Shimadzu 2014 with Rt-Qplot capillary column [length 30 m, ID 0.32 mm]) and GC/mass spectroscopy (MS) (Thermo-Scientific with TG-5MS capillary column [length 30 m, ID 0.25 mm]). Second, the total organic carbon analyzer (Shimadzu, TOC-L series, Japan) was used to quantitatively analyze the obtained liquid samples at the end of each run [15–17], and the Nash approach [12, 18, 19]

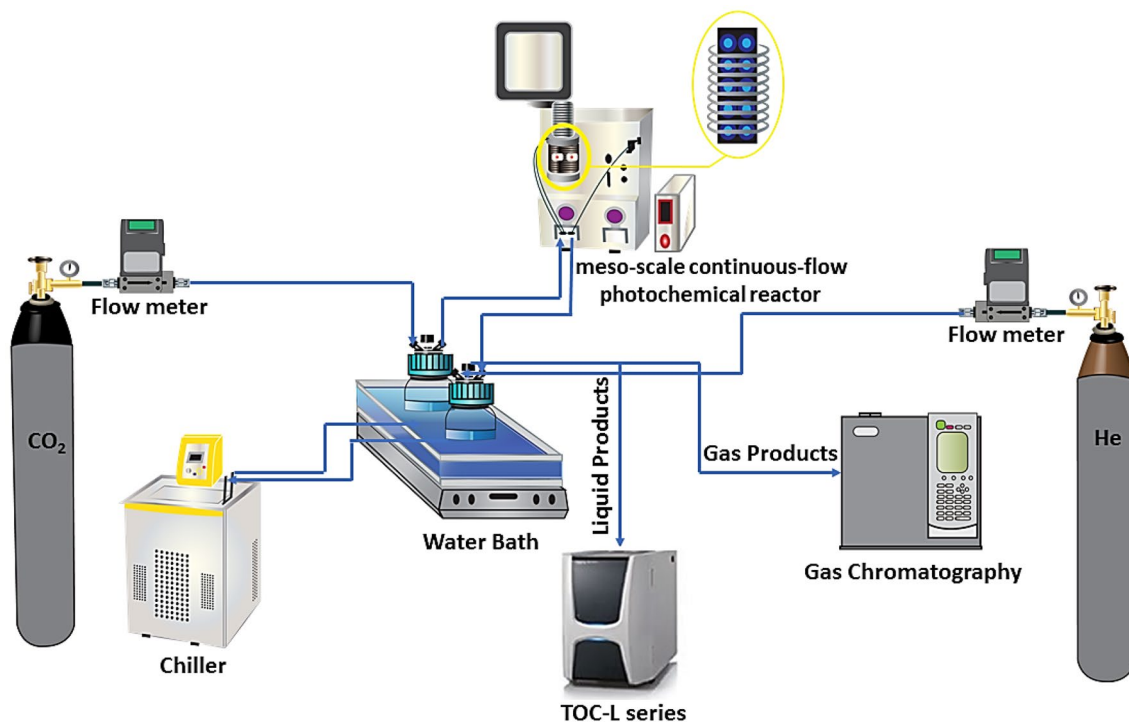


Fig. 1 The experimental setup scheme

was employed to determine the formaldehyde quantity at an absorbance wavelength of 414 nm. There were no TOC or formaldehyde identified in the blank samples.

3 Results and Discussion

3.1 Photocatalysts Characterization

Figure 2a–d and f–h present the morphology of the synthesized photocatalysts with both TEM and HAADF-STEM images.

It is well noticed that the shape of T1 is typical to the spherical nanoparticles with a particle size varying from 14.04 nm to 26.78 nm as exhibited in Fig. 2a. Figure 2e is the HRTEM image for the T1 nanoparticles which illustrates the lattice fringes with a spacing of 0.35 nm at scale 2 nm which is corresponding to (101) anatase TiO₂.

Figure 2b shows the well disperse of Pt NPs on the surface of TiO₂ nanoparticles and the particle size of Pt NPs were varying from 4.35 nm to 6.13 nm. In addition, Fig. 2c, d illustrates the uniform and homogenous distribution of both Pt NPs and RGO sheets on the surface of T1 and T2, respectively. The HAADF-STEM images confirm the results obtained by TEM.

Furthermore, to study the elemental analysis and weight percentage of each nanocomposite, an energy-dispersive X-ray spectroscopy (JEOL JEM-2100F) was used to perform EDX. The analysis proved the existence of titanium, oxygen, carbon, and platinum in the photocatalysts as demonstrated in Fig. 2i–l. The Ti and O elements were derived from TiO₂ nanoparticles while C element was from the presence of RGO sheets and Pt peaks confirmed the existence of Pt element in the nanocomposites. The actual weight percentage of the doped Pt in each nanocomposite is shown in Table 1.

XRD patterns were used to investigate the phase and crystalline composition of all produced nanocomposites, and the findings are exhibited in Fig. 3. For both the tetragonal anatase and tetragonal rutile phases of TiO₂, all peaks were compared to the Joint Committee on Powder Diffraction Standards (JCPDS) Card File no. 00-002-0387 and Card File no. 00-001-1292, respectively. The anatase phase of TiO₂ diffraction peaks exist at $2\theta = 25.18^\circ, 37.72^\circ, 38.42^\circ, 47.95^\circ, 53.90^\circ, 54.26^\circ, 62.60^\circ, 68.73^\circ, 70.14^\circ, 74.99^\circ$ matches with (101), (103), (004), (200), (105), (211), (204), (116), (220), (215) crystal facets of anatase phase, respectively. Whereas the diffraction peaks of rutile TiO₂ appears at $2\theta = 27.32^\circ, 36.82^\circ, 38.82^\circ, 41.18^\circ, 55.90^\circ$ corresponding to (110), (101), (200), (111), (211) crystal facets of rutile phase, respectively. Pt NPs were insignificant to be detected using XRD detection limit so that diffraction peaks of TiO₂ did not change after Pt NPs were loaded on its surface.

Scherrer's equation was used to measure the average crystallite size of samples based on the maximum three peaks of the anatase and rutile phases.

$$L = K\lambda/\beta\cos\theta \quad (1)$$

where L represents the crystallite size (nm), K expresses a constant which equals to 0.9 in this case and it depends on the crystallite shape, whereas the X-ray wavelength (nm) is referred to by λ , β means the full width at half maximum (FWHM) and θ demonstrates the Bragg's angle.

The relative peak intensity of anatase and rutile was used to calculate the phase composition of the samples [20, 21].

$$F_A = 1/[1 + 1.26(I_R/I_A)] \quad (2)$$

where the fraction of anatase phase is referred to by F_A whereas I_R and I_A are the intensity of the rutile (110) and anatase (101) diffraction peaks, respectively. Table 1 summarizes the calculated crystallite size and phase composition for both anatase and rutile phases of all photocatalysts.

It is well obvious from Table 1 that the crystallite size i.e. the degree of crystallinity for anatase phase increased with the addition of Pt NPs and RGO to TiO₂ samples. The same result was mentioned by Ola et al. [22] for the noble metal loading. Meanwhile, for 0.3 wt.% PTG2, the degree of crystallinity for rutile phase decreased comparing with T2.

Also, the percentage of the rutile phase in 0.3 wt.% PTG1 composite was slightly increased after the introduction of RGO and Pt NPs compared with T1. The same observation of the anatase transformation to rutile was previously reported during other metals loading and the introduction of RGO on TiO₂ surface especially with the temperature elevation such as in this case with the hydrothermal reaction [23–26]. While in the case of 0.3 wt.% PTG2 composite the (anatase: rutile) ratio was maintained at the same value as T2.

This may be related to the microstructure of TiO₂ which has three types such as the individual structure of anatase and rutile phases, heterojunction structure involving rutile clusters overlaid on anatase nanoparticles and the inter-particles structure [23]. It was mentioned that the (anatase/rutile) ratio would decrease during the hydrothermal reaction if they existed individually [23].

To further test the chemical bonds and functional groups of catalysts, FTIR for catalysts were performed and the results are displayed in Fig. 4.

It is well seen that there are eight distinguished absorption bands in the FTIR spectrum region from 450 cm⁻¹ to 4000 cm⁻¹. The Ti–O–Ti and Ti–O–C stretching vibrations are laid in the absorption bands below 1000 cm⁻¹. The existence of absorption band at 1075 cm⁻¹ is due to the stretch vibrations for C–O group which attributed to epoxy or alkoxy groups whereas the peak at 1250 cm⁻¹ was

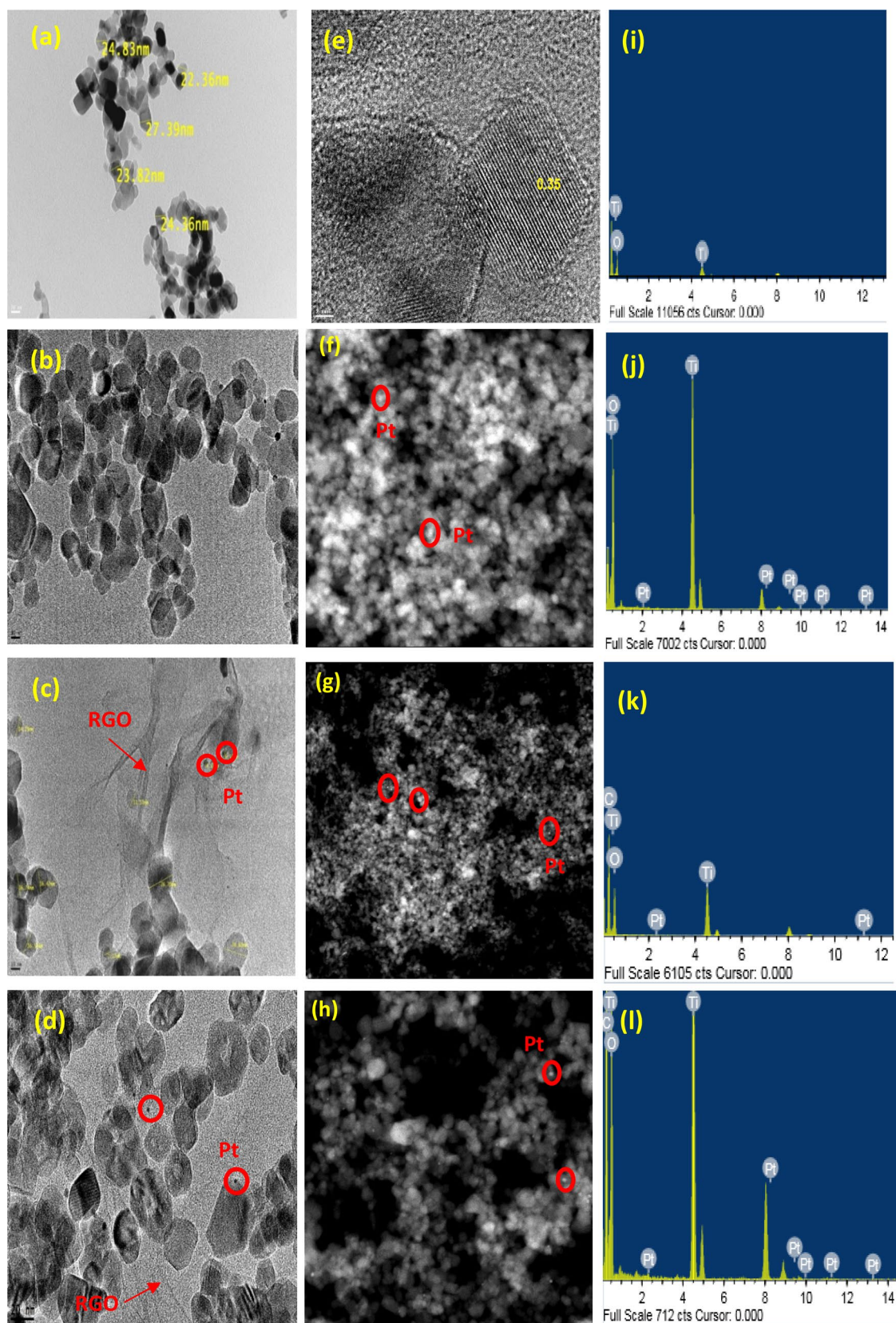
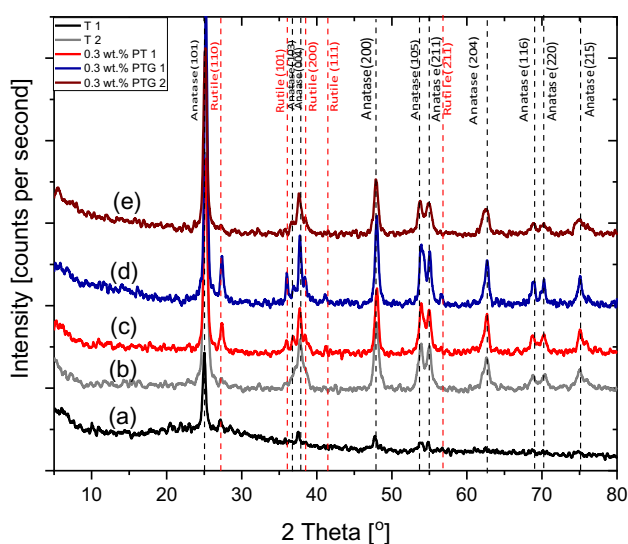


Fig. 2 a,e,i are TEM, HRTEM, EDX for T1 while typical TEM, HAADF-STEM, EDX characterizations of b,f,j for PT1, c,g,k for PTG1, and d,h,l for PTG2, respectively

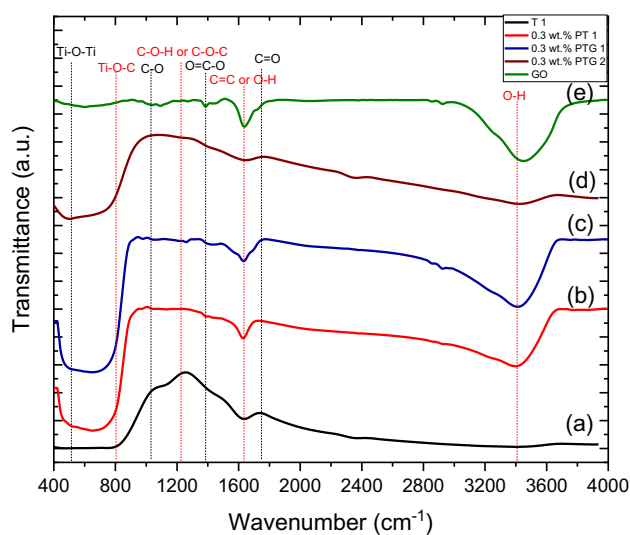
Table 1 The EDX elemental analysis and XRD of the synthesized photocatalysts

Sample	EDX analysis (wt.%)				XRD analysis	
	Ti	O	Pt	C	Phase composition	Crystallite size (nm)
T1	62.64	37.36	0	0	Anatase (77%) Rutile (23%)	15.1 18.3
T2	64.50	35.50	0	0	Anatase (81%) Rutile (19%)	13.2 17.7
0.3 wt.% PT1	62.50	37.25	0.25	0	Anatase (76%) Rutile (24%)	15.7 19.4
0.3 wt.% PTG1	23.69	19.67	0.28	56.36	Anatase (75%) Rutile (25%)	19.6 19.9
0.3 wt.% PTG2	27.82	21.72	0.30	50.16	Anatase (81%) Rutile (19%)	15.9 10.9

**Fig. 3** XRD pattern for **a** T1, **b** T2, **c** 0.3 wt.% PT1, **d** 0.3 wt.% PTG1 and **e** 0.3 wt.% PTG2

assigned to epoxide C–O–C or phenolic C–O–H stretching vibrations. The peaks at 1395 cm^{-1} , 1730 cm^{-1} and 3400 cm^{-1} belong to carboxyl group $\text{O}=\text{C}-\text{O}$, carbonyl $\text{C}=\text{O}$ and hydroxyl group OH , respectively. Finally, the absorption band at 1630 cm^{-1} , in case of TiO_2 and Pt/TiO_2 catalysts, it may refer to the associated water adsorbed on the particle surfaces while in case of $\text{Pt/TiO}_2/\text{RGO}$, it is well obvious that the intensity of the band increased which may be attributed to $\text{C}=\text{C}$ stretching vibration which represent the skeletal vibrations of unoxidized graphitic domains located at the same absorption band.

The existence of $\text{Ti}-\text{O}-\text{C}$ bond confirms that through the synthesis of $\text{Pt/TiO}_2/\text{RGO}$ using hydrothermal reduction method, GO with the residual $\text{O}=\text{C}-\text{O}$ groups reacted with the surface hydroxyl groups $\text{O}-\text{H}$ of TiO_2

**Fig. 4** FTIR for **a** T1, **b** 0.3 wt.% PT1, **c** 0.3 wt.% PTG1, **d** 0.3 wt.% PTG2, and **e** GO

NPs resulting in forming a chemical bonded TiO_2/RGO , similar results are reported elsewhere [4, 27].

The effect of RGO and Pt NPs addition on the composites' specific surface area, BET surface area and Barrett-Joyner-Halenda (BJH) porosity of T1, T2, 0.3 wt. % PT1, 0.3 wt. % PTG1 and 0.3 wt. % PTG2 had been performed. Results are illustrated as demonstrated in Fig. 5.

Table 2 illustrates both the Brunauer–Emmett–Teller (BET) specific surface area and pore volume for all photocatalysts.

It is well noticed from Table 2 that the specific surface area rises with increasing both of metal loaded nanoparticles and RGO sheets that was in agreement with previous studies [22].

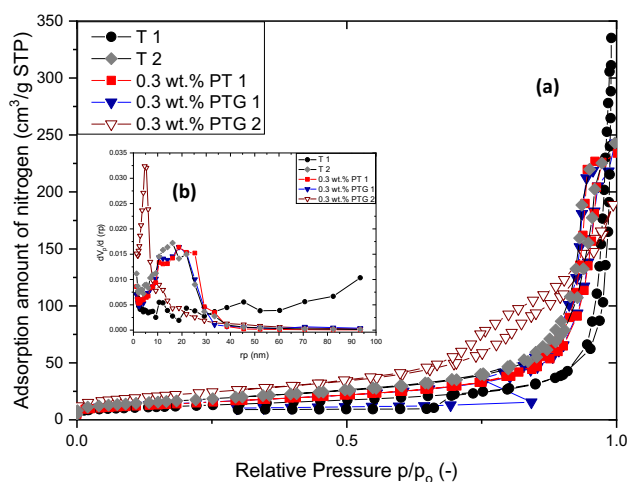


Fig. 5 N_2 adsorption/desorption isotherms at 77 K (a) and pore size distribution curve (b) for all synthesized photocatalysts

Table 2 BET surface area, pore volume and the optical properties for all photocatalysts

Sample	N_2 adsorption/desorption analysis		(DRS) analysis
	BET Surface area (m^2/g)	BJH adsorption pore volume (cm^3/g)	Band gap (eV)
T1	46.66	0.4968	3.00
T2	52.41	0.212	3.11
0.3 wt.% PT1	50.33	0.357	2.75
0.3 wt.% PTG1	53.38	0.3529	2.69
0.3 wt.% PTG2	78.14	0.284	2.72

As shown in Fig. 5-a, the initial portion of adsorption isotherms at low relative pressure (P/P_0) represents the formation of monolayer adsorption on the photocatalyst surfaces then the increment of adsorption volume with the relative pressure increase exhibits the formation of multilayer adsorption leading to spontaneously condensation of gas into liquid-like state inside the photocatalyst pores which is called capillary condensation phenomenon. Therefore, it is well obvious that all the photocatalysts exhibit IV adsorption–desorption isotherm type representative of mesoporous materials agreeing with IUPAC classification with H1 hysteresis loops except the 0.3 wt.% PTG2 photocatalyst shows a H3 hysteresis loop.

The pore diameter of T1, T2, 0.3 PT1, 0.3 wt.% PTG1 and 0.3 wt.% PTG2 were 46.184 nm, 35.54 nm, 28.369 nm, 26.64 nm and 14.56 nm respectively.

The optical features of photocatalysts were examined using the UV–Vis (diffuse reflectance spectra) as demonstrated in Fig. 6. From (DRS) figure (a), it is clear that adding of noble metal (Pt NPs) slightly improves the visible light absorbance. Furthermore, introducing of RGO sheets further boosts the red shift of the absorption edge. This may be owing to the existence of Ti–O–C bond between TiO_2 and RGO [14]. Similar observations were reported in literature [4, 10, 14, 28]. The band gap calculations were performed from the plots of Kubelka–Munk function versus the photon energy as exhibited in Fig. 6b and Table 2. It was noticed that the band gap of T1 is smaller than T2 catalyst. As mentioned in Table 2, the band gaps were 3.00 eV and 3.11 eV for T1 and T2, respectively. Even after the introduction of Pt NPs and RGO sheets, the band gap was 2.69 eV for 0.3 wt.% PTG1 and 2.72 eV for 0.3 wt.% PTG2. As reported in

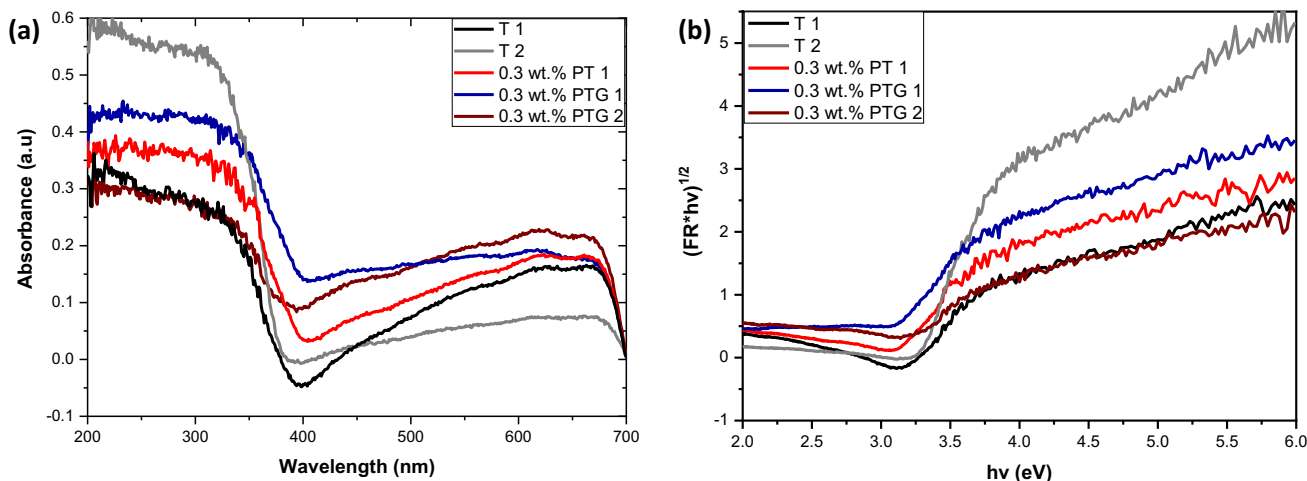


Fig. 6 UV–Vis spectra (a) and transformed Kubelka–Munk function versus the photonic energy (b) for all samples

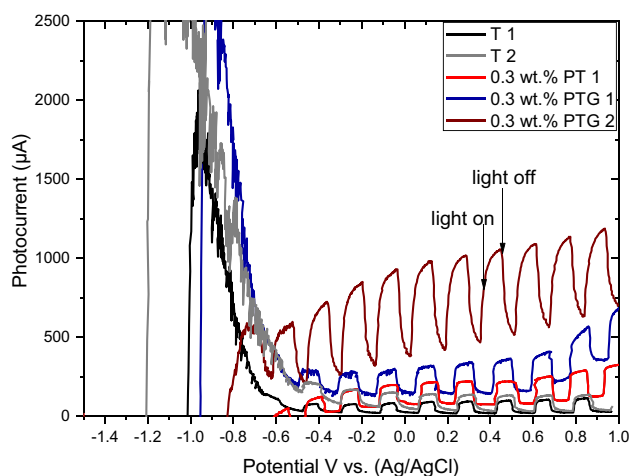


Fig. 7 Photocurrent-potential response (LSV) for the prepared photocatalysts under numerous on/off cycles

the literature, the band gap of pure anatase is equal (3.23 eV) and for pure rutile is (3.02 eV). It is well noted that (anatase: rutile) ratio influences the position of band gaps of metal-TiO₂ samples. In this case, the 0.3 wt.% PTG1 has a ratio of (anatase: rutile) equal to (75:25) and its band gap is 2.69 eV while 0.3 wt.% PTG2 has (81:19) ratio and a band gap of 2.72 eV. The same observation was reported by Dubey et al. [28].

3.2 Photoelectrochemical Measurements (PEC)

The optoelectronic performance of the synthesized photocatalysts was investigated using the photoelectrochemical measurements. The photocurrent-potential response (linear sweep voltammetry, LSV), Transient photocurrent response (chronoamperometry CAM), and (electrochemical impedance spectroscopy EIS) were conducted in a three-electrode cell filled with 0.1 M aqueous Na₂SO₄ solution after 30 min purging with Ar gas. After deposition of catalysts using the (EPD) technique, the working electrode (W.E) was utilized in the PEC measurements even with no further treatment such as necking or heating.

The LSV was carried out in the presence of chopped illumination within range of (-1.5 V to 1 V) and the results are displayed in Fig. 7. The instantaneous photocurrent response via several light on cycles and the subsequent discharge due to the light off cycles confirms the stability of electrodes and the effective separation of electron-hole pairs of catalysts [14, 29, 30].

Figure 7 shows that all composites exhibit an anodic photocurrent response which proves the n-type semiconductor characteristics. Also, adding of Pt NPs and RGO sheets increase the photocurrent thus improve the photoactivity.

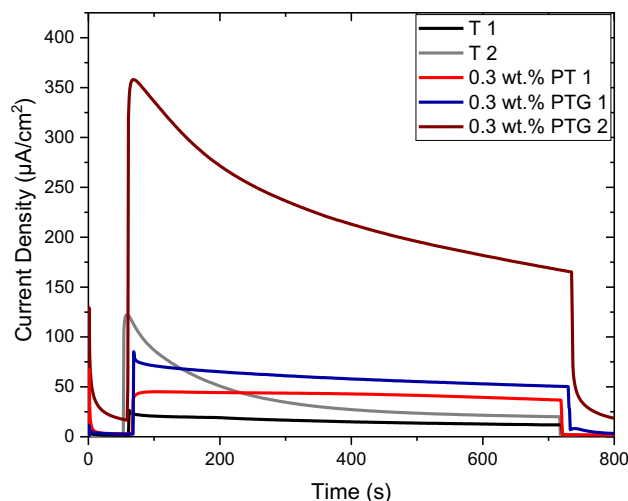


Fig. 8 Chronoamperometry (CAM) of the prepared photocatalysts at +0.6 vs. Ag/AgCl in 0.1 M Na₂SO₄ electrolyte under UV LED light irradiation (365 nm)

Meanwhile, it is well clear that the 0.3 wt.% PTG2 composite exhibits an increase in the photocurrent response approximately 2 times higher than 0.3 wt.% PTG1. Moreover, the anodic photocurrent transient profile of 0.3 wt.% PTG2 composite shows a triangular pattern (after turning the light off) that differs from the rectangular pattern of the other composites. The same triangular pattern in the charge-discharge cycles was observed for the ideal capacitors [14] which reveals that the 0.3 wt.% PTG2 composite has a superior activity to other photocatalysts. This could be ascribed to the better reproducibility of electrons and effective separation of the photogenerated charges and holes.

To evaluate the transient photocurrent responses of the photocatalysts, the chronoamperometry measurement was performed at (+0.6 vs. Ag/AgCl) for 800 s divided into three sections. The first section included 60 s in dark then the second section involved lighting on for 600 s and finally shutting off the light until the measurement was completed as displayed in Fig. 8.

As shown from Fig. 8, all photocatalysts samples exhibited an efficient response towards the transient photocurrent while the superior photocurrent density was recorded by the ternary composites of PTG1 and PTG2 that confirm results observed in the LSV. Also, similar results were reported for the binary and ternary composites with [29] and [9]. This may be assigned to the efficient electron-hole separation due to electrons trapping by Pt NPs and the decrease of the recombination in the ternary nanocomposites.

Moreover, the ternary composite of PTG2 had an efficient photocurrent density comparing to PTG1 which confirms the proficiency of the T2 over T1 photocatalyst. This result could be ascribed to the increase of BET surface area of the T2 over T1.

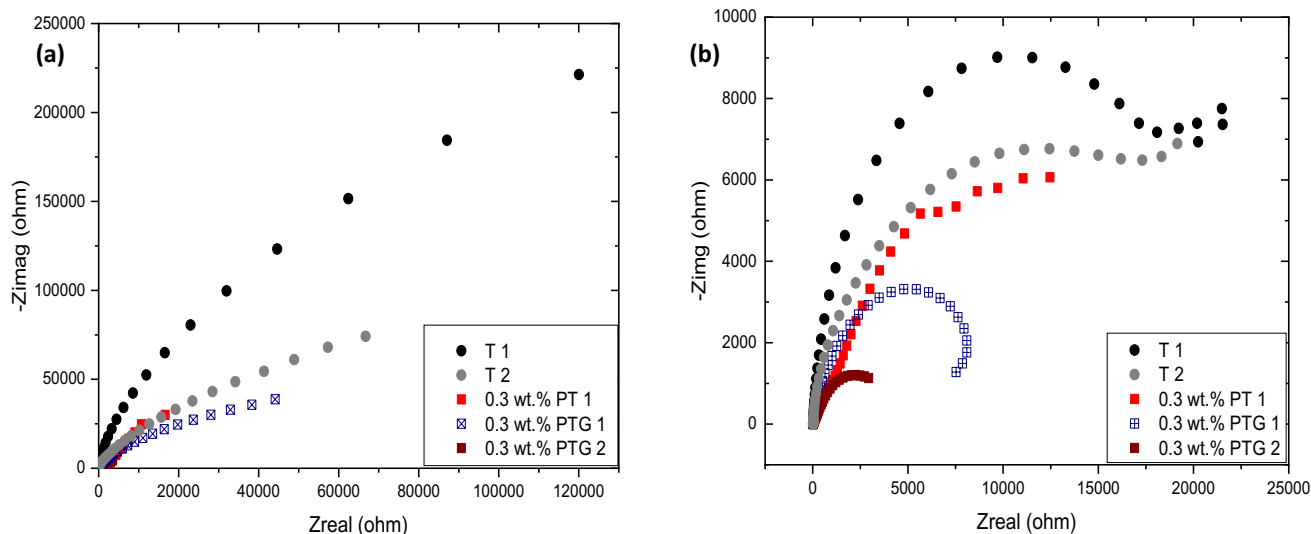


Fig. 9 Nyquist plots of EIS for T1, T2, 0.3 wt.% PT1, 0.3 wt.% PTG1, 0.3 wt.% PTG2 in 0.1 M Na₂SO₄ solution, in dark (a), and light illumination ($\lambda = 365$ nm) (b) at 0.0 V (vs. Ag/AgCl)

The (EIS) is a convenient way to examine the electrons transfer and the recombination process at the interface of semiconductor/electrolyte [31]. The values of (EIS) of all catalysts in both the dark and light illumination conditions ($\lambda = 365$ nm) are exhibited in Nyquist plots and shown in Fig. 8. The analyses were conducted in 0.1 M Na₂SO₄ solution at frequencies varying from 100 kHz to 0.01 Hz and at 0.0 V (vs. Ag/AgCl).

As previously explained in literatures [14, 31, 32], the intersection between the first point of the arc which located at the region of high frequency and the real impedance (Z_{real}) represents the bulk resistance between (W.E) and (R.E) or the equivalent series resistance (ESR). While the intermediate section of frequency where the semicircular arc is located, the intercept with (Z_{real}) shows the charge transfer resistance (R_{CT}). Thus, a smaller impedance arc radius indicates a smaller (R_{CT}) across the electrode/electrolyte interface [31]. Therefore, a higher electronic conductivity, the maximum photocatalytic efficiency and a minimal electron–hole recombination could be achieved [9, 30, 33].

As well seen from Fig. 8, the 0.3 wt.% PTG2 composite has the superior photocatalytic efficiency to the other catalysts. This illustrates that 0.3 wt.% PTG2 composite has the capability of the fast electrons transfer consequently decreasing the recombination process (Fig. 9).

3.3 Parameters Affecting the Photoreduction of CO₂

The CO₂ photoreduction is highly influenced by numerous parameters such as (i) type of photocatalyst used,

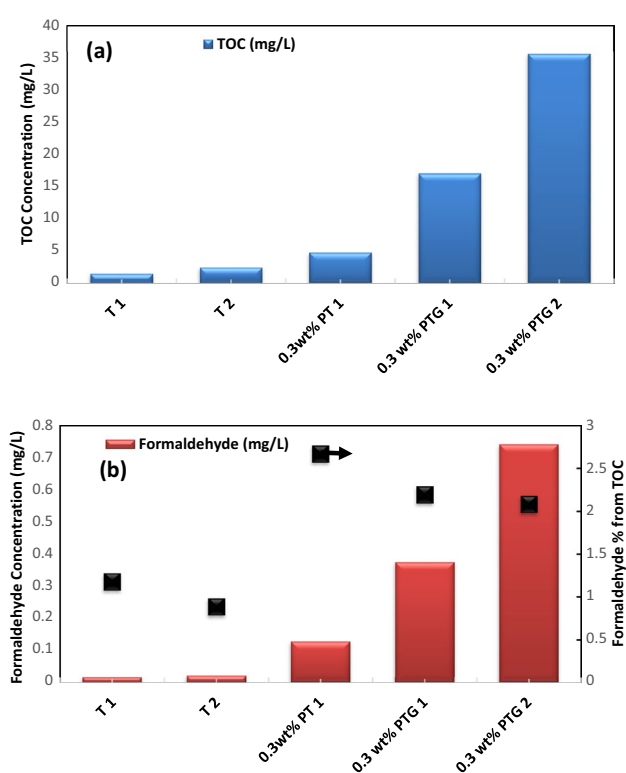


Fig. 10 Effect of the catalyst type on **a** TOC concentration **b** Formaldehyde concentration and formaldehyde% in TOC, (Photocatalyst weight = 30 mg, deionized water volume = 65 ml, liquid pump flow rate = 500 μ l/min and reactor temperature = 30 °C)

(ii) weight of photocatalyst utilized, (iii) photochemical reactor temperature, (iv) retention time inside the photochemical reactor, and (v) content of cocatalyst loading.

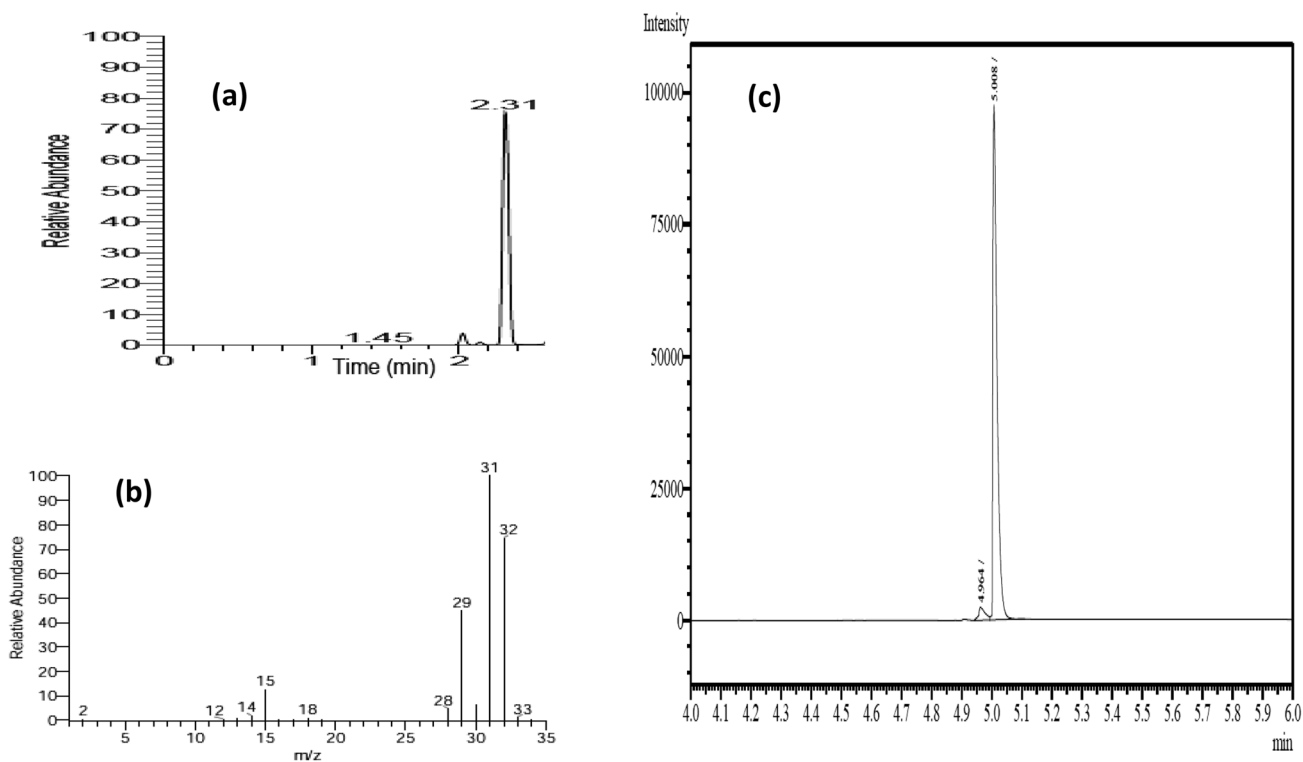


Fig. 11 Analysis for one of the samples confirms the presence of methanol **a** The chromatographic peak corresponding to methanol on GC/MS, **b** MS spectrum on GC/MS, and **c** The chromatographic peak corresponding to methanol on GC/FID

Here in this study, all these factors were examined using the previously mentioned flow type photochemical reactor as in Fig. 1.

3.4 Effect of the Catalyst Type

In order to investigate the effect of catalyst type, first we will examine the effect of the presence of both RGO and Pt as a cocatalyst then we will investigate the effect of (anatase: rutile) ratio. Figure 10 shows the variation in both TOC and formaldehyde concentrations with different catalysts.

It is well notice that the introduction of Pt NPs and RGO sheets increases the concentration of TOC as well as formaldehyde which enhances the photoreduction of CO_2 . As shown with 0.3 wt.% PTG1 composite, the Pt loading as a cocatalyst improves the photoactivity owing to Schottky barrier formation between TiO_2 and Pt NPs which acts as electrons trap and hinders the recombination [34] thus increases the photoreduction of CO_2 . Also, the introduction of RGO sheets contributes to the simple movement of photogenerated electrons from TiO_2 to RGO as well as the perfect electronic conductivity of RGO because of the 2D and planar π -conjugation structure [5, 14].

Meanwhile, the percentage of formaldehyde in TOC was still too low, and the maximum percentage was (2.7) of

TOC. This confirms the results obtained by GC/MS and GC/FID which illustrates that methanol was the main product as shown in Fig. 11

From Fig. 10, it is well obvious that 0.3 wt.% PTG2 enhances the concentration of both TOC and formaldehyde more than those obtained by 0.3 wt.% PTG1 while the formaldehyde percentage in TOC was still too low which may be attributed to the formation of other organic compounds i.e. methanol. The superior photoactivity of 0.3 wt.% PTG2 photocatalyst was previously noted in the PEC measurements section.

This superior activity of 0.3 wt.% PTG2 might be explained according to the results obtained from the previous sections of XRD and BET surface area which demonstrated that (anatase: rutile) ratio and the surface area were (81: 19), 78.14 (m^2/g) while they were (75:25), 53.38 (m^2/g) for 0.3 wt.% PTG2 and 0.3 wt.% PTG1, respectively.

It seems that (anatase: rutile) ratio shows an essential role in photocatalytic activity. It was previously reported that rich anatase/rutile content had a superior photoactivity for CO_2 photocatalytic reduction [35] which is in agreement with our case.

Also, it was confirmed that the anatase phase is highly activity compared with the rutile phase in many reactions [36]. It was also found that a small amount of rutile added

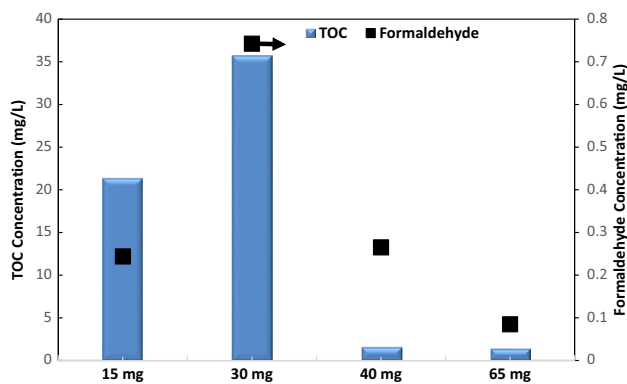


Fig. 12 Effect of the catalyst weight on TOC and formaldehyde concentration, (0.3 wt.% PTG2, deionized water volume=65 ml, liquid pump flow rate=500 μ l/min and reactor temperature=30 $^{\circ}$ C)

to the anatase phase may hinder the recombination of photogenerated holes and electrons, therefore, enhances the photocatalytic activity [37].

Furthermore, it was reported that the surface area of TiO_2 has an effective role in the CO_2 photoreduction as the increase of TiO_2 BET surface area specially the anatase (101) facet could improve the adsorption capacity of CO_2 on TiO_2 surface [38, 39].

We could conclude that the rich of (anatase: rutile) ratio and the increase of BET surface area are the major reasons for the enhancement of CO_2 reduction in the case of 0.3 wt.% PTG2. This may be attributed to the lower recombination of the photogenerated electrons and holes as well as the high adsorption capability of the surface of anatase phase [35, 38].

3.4.1 Effect of the Weight of Catalyst Utilized

Figure 12 illustrates the effect of catalyst weight on TOC and formaldehyde concentrations.

As shown from the previous figure, the increase of the catalyst weight increases the TOC and formaldehyde concentrations up to 30 mg then any additional increase of the catalyst weight decreases both TOC and formaldehyde concentrations. This could be explained due to the formation of an adhesive layer from the catalyst on the inner surface of the photochemical reactor channels (ID=1.3 mm) which limits the penetration of light and consequently the light absorption especially with the use of low liquid flow rate, therefore, decreases the photocatalytic reduction of CO_2 .

3.4.2 Effect of the Photochemical Reactor Temperature

Figure 13 depicts the effect of reactor temperature on the concentrations of TOC and formaldehyde. As the temperature of the reaction rises by 10 $^{\circ}$ C, from 30 $^{\circ}$ C to 40 $^{\circ}$ C,

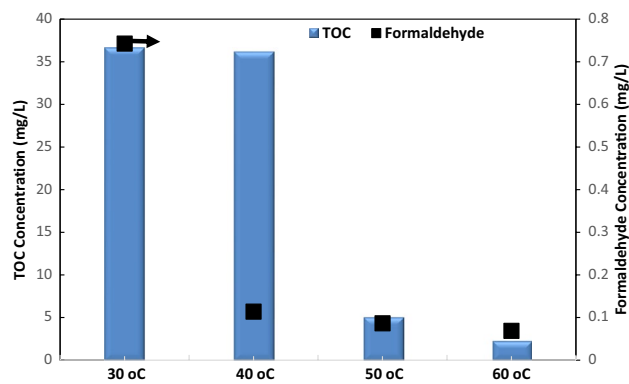


Fig. 13 Effect of the reactor temperature and on TOC and formaldehyde concentration, (0.3 wt.% PTG2, photocatalyst weight=30 mg, deionized water volume=65 ml and liquid pump flow rate=500 μ l/min)

the TOC concentration remains constant. This result is in consistent with Fox et al. [40] and Kočí et al. [41], who confirmed that the photocatalytic reactions are not affected by the small variations in temperature.

While increasing the temperature to higher values may greatly influence on the photocatalytic reaction of CO_2 . To explain the present results, it should be mentioned that the elevation of temperature in any gas–liquid–solid system leads to two consequences: on one hand, the rate of the chemical reaction and the kinetic rate constants are usually increased exponentially with temperature. On the other hand, the elevation of temperature determines the equilibrium amount of dissolved CO_2 [41]. It is well obvious that the predominating effect at 50 $^{\circ}$ C is the adverse effect so that the TOC concentration decreased.

Whereas the formaldehyde concentration is generally decreasing with the elevation of temperature which indicates the formation of other organics.

3.4.3 Effect of Liquid Flow Rate

We choose 0.3 wt.% PTG2 as a catalyst, 30 mg for the weight of catalyst and 30 $^{\circ}$ C for the photochemical reactor temperature now we will examine the effect of retention time by changing the liquid pump flow rate. The retention time inside the flow type photochemical reactor could be calculated by this equation:

$$\text{Retention time} = \frac{\text{reactor volume}}{\text{liquid pump flow rate}} \quad (3)$$

Figure 14 shows the effect of liquid flow rate and consequently the retention time in the photochemical reactor on TOC and formaldehyde concentrations.

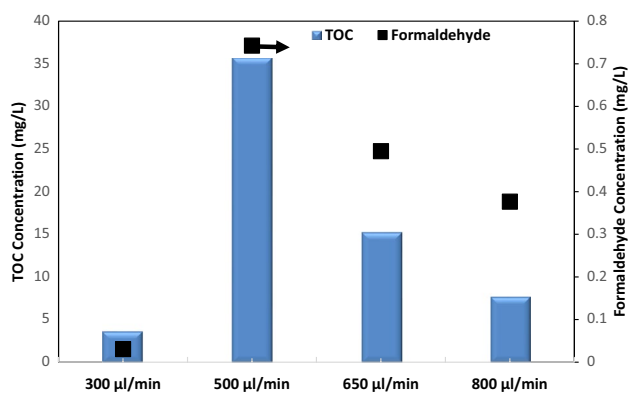


Fig. 14 Effect of liquid flow rates on TOC and formaldehyde concentrations, (0.3 wt.% PTG2, photocatalyst weight=30 mg, deionized water volume=65 ml and photochemical reactor temperature = 30 °C)

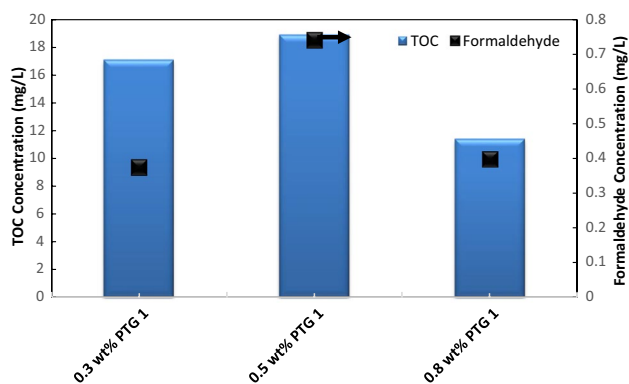


Fig. 15 Effect of cocatalyst loading on TOC and formaldehyde concentrations, (Photocatalyst weight=30 mg, deionized water volume=65 ml and photochemical reactor temperature=30 °C and liquid pump flow rate=500 µl/min)

As noted in Fig. 14, the maximum concentrations for both TOC and formaldehyde were obtained at 500 µl/min (retention time = 20 min.).

As known, increasing the retention time by decreasing the liquid flow rate may be beneficial for the photoreduction of CO₂. Meanwhile, in this case lowering the liquid flow rate to 300 µl/min decreases the TOC as well as formaldehyde concentrations. This may be attributed to the insufficient CO₂ and water (OH⁻) supplied to the photochemical reactor so that decreasing TOC and formaldehyde. Moreover, increasing time inside the reactor may cause oxidation for the generated organics lowering the TOC and formaldehyde concentrations as well. The same result was reported by Cheng et al. [42] and Kalamaras et al. [43].

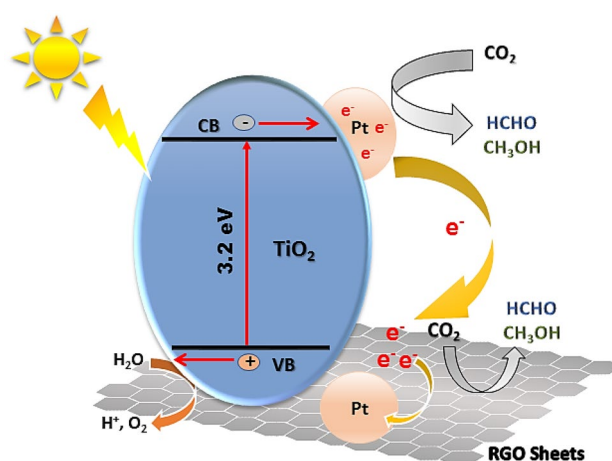


Fig. 16 Proposed CO₂ photoreduction mechanism over Pt/TiO₂ and Pt/TiO₂/RGO nanocomposites

3.4.4 Effect of Cocatalyst Loading

Herein, we will investigate the effect of loading amounts of Pt as a cocatalyst by using T1 as a semiconductor. The operating conditions in this case would be 30 °C for the photochemical reactor temperature, 500 µl/min for the liquid flow rate and 30 mg from each catalyst. Figure 15 shows the effect of Pt loading as a cocatalyst.

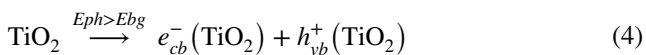
As noted from Fig. 15 the excess of Pt NPs loading on TG1 composite surface negatively affects CO₂ photocatalytic reduction. This finding is agreement with the previously reported studies [7, 8, 44]. These results may be due to the increase of the recombination of the photoexcited charges which hinder the reduction of CO₂ as the too large amount of Pt NPs may lead to a shorter distance between the photogenerated electrons and holes [7]. It was also reported that a certain amount of noble metal loaded on TiO₂ photocatalyst could enhance the photoreduction of CO₂. However, the excess of loading covers the TiO₂ surface thus inhibit the excitation of electrons therefore declines the photoreduction of CO₂ [8].

The optimum amount of Pt loading which enhances the concentration of TOC and formaldehyde in this case was 0.5 wt.% PTG1 as depicted in Fig. 15.

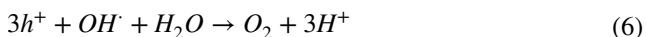
4 Photocatalytic CO₂ Reduction Mechanism

The mechanism of CO₂ photoreduction firstly starts with the absorption of CO₂ gas in liquid H₂O. Secondly, the adsorption of CO₂ and H₂O molecules takes place on TiO₂ surface. As the light strikes on the TiO₂ surface with sufficient photonic energy ($h\nu >$ band gap energy of the semiconductor), electrons jump from the valence band (VB) [O 2p orbital]

to the conduction band (CB) [Ti 3d orbital] [5, 10], as displayed schematically in Fig. 16 and illustrated in Eq. (4):

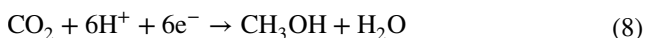
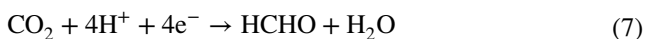


Holes in (VB) react with the adsorbed H_2O molecules on the surface of TiO_2 to form both hydroxyl radicals (OH^\cdot) and hydrogen ions (H^+) then further oxidation occurs by OH^\cdot radicals to emit O_2 and H^+ .



As shown in Fig. 16, in case of Pt/ TiO_2 composite, the presence of Pt NPs on the surface of TiO_2 leads to Schottky barrier formation at the interface which aids the separation of photoexcited electrons and improves the trapping of electrons resulted in preventing the recombination of charges. In case of Pt/ TiO_2 /RGO composite, the photogenerated charges from the (CB) of TiO_2 could transfer to RGO sheets across the two-dimensional carbon network then trapped by Pt NPs. The RGO sheets offer a large surface area and enhance the conductivity of electrons. Moreover, RGO sheets acted as a support to provide a high Pt NPs dispersion which inhibits the aggregation of Pt NPs thus enhance the CO_2 photocatalytic reduction [10].

The possible reactions of the excited electrons with the adsorbed CO_2 to produce liquid organic carbons such as formic acid, formaldehyde, and methanol are described by Eqs. (7, 8, 9) [19]:



5 Conclusion

In this study, graphene oxide (GO) was prepared using modified Hummers' method. A hydrothermal method was employed to synthesize binary (PT) and ternary composites (PTG1 and PTG2). The use of graphene in PTG1 photocatalyst enhanced the TOC by 3.5 and 11.4 times compared with PT1 and T1, respectively using the proposed photochemical reactor in a continuous mode. Furthermore, the effect of (anatase: rutile) ratio was examined by comparing the two kinds of ternary composites. Results revealed that compared to other photocatalysts, the 0.3 wt.% PTG2 photocatalyst,

which possessed the (anatase: rutile) ratio of (81:19) and a surface area of 78.14 (m^2/g) gave the supreme photocatalytic activity approximately 2 times higher than PTG1, in both the photocurrent generation via PEC measurements and CO_2 photoreduction.

Additionally, to achieve higher TOC concentrations, the operating parameters for the advanced meso-scale continuous flow photochemical reactor were investigated. The optimum conditions were found as 500 $\mu\text{l}/\text{min}$ for the water flow rate, 30 $^\circ\text{C}$ and 40 $^\circ\text{C}$ for the reactor temperature, and 30 mg for the weight of catalyst utilized. The maximum amount of Pt loading to enhance CO_2 photocatalytic reduction was 0.5 wt.% Pt over TG1.

Finally, we could conclude that the rich of (anatase: rutile) ratio, the increase of BET surface area along with operating the photochemical reactor under the optimum conditions are the key reasons for the enhancement of CO_2 reduction and the production of valuable organic compounds.

Acknowledgements The author, S. Nabil, gratefully acknowledges the Egypt-Japan University of Science and Technology (E-JUST), especially the TMD (Technology Management Department), for providing the facilities and support to accomplish this work.

Author Contributions All authors contributed to the study conception and design. Material preparation, data collection and analysis were performed by [SN]. Monitoring and advice to accomplish this research was done by [Prof. MFE]. [Prof. YM] supplied the UV lamp and its setup to perform the PEC measurements. The supervision, discussion of results and suggestion of the research point were performed by [Prof. EAS], and [Prof. AHE-S]. The first draft of the manuscript was written by [SN] and all authors commented on previous versions of the manuscript. All authors read and approved the final manuscript.

Funding Open access funding provided by The Science, Technology &. The analysis of all samples as well as all experiments were conducted in the laboratories of Egypt-Japan University of Science and Technology (E-JUST).

Data Availability All data generated or analyzed during this study are included in this published article.

Declarations

Conflict of Interest On behalf of all authors, the corresponding author states that there is no conflict of interest.

Ethical Approval and Consent to Participate The manuscript does not involve the use of any animal or human data or tissue. "Not applicable".

Consent for Publication The manuscript does not contain data from any individual person. "Not applicable".

Open Access This article is licensed under a Creative Commons Attribution 4.0 International License, which permits use, sharing, adaptation, distribution and reproduction in any medium or format, as long as you give appropriate credit to the original author(s) and the source, provide a link to the Creative Commons licence, and indicate if changes

were made. The images or other third party material in this article are included in the article's Creative Commons licence, unless indicated otherwise in a credit line to the material. If material is not included in the article's Creative Commons licence and your intended use is not permitted by statutory regulation or exceeds the permitted use, you will need to obtain permission directly from the copyright holder. To view a copy of this licence, visit <http://creativecommons.org/licenses/by/4.0/>.

References

- Zhuo Xiong CZ, Wang Haibing, Nuoyan Xu, Li Hailong, Fang Baizeng, Zhao Yongchun, Zhang Junying (2015) Photocatalytic reduction of CO₂ on Pt₂pePtO/TiO₂ nanoparticles under UV/Vis light irradiation: a combination of Pt₂p doping and Pt nanoparticles deposition. *Int J Hydrogen Energy* 40:10049–10062. <https://doi.org/10.1016/j.ijhydene.2015.06.075>
- Wang B et al (2018) Recent progress in the photocatalytic reduction of aqueous carbon dioxide. *Catal Today* 311(October):23–39. <https://doi.org/10.1016/j.cattod.2017.10.006>
- Li K, An X, Park KH, Khraisheh M, Tang J (2014) A critical review of CO₂ photoconversion: catalysts and reactors. *Catal Today* 224:3–12. <https://doi.org/10.1016/j.cattod.2013.12.006>
- Zhao Y et al (2018) (2017) Graphene-wrapped Pt/TiO₂ photocatalysts with enhanced photogenerated charges separation and reactant adsorption for high selective photoreduction of CO₂ to CH₄. *Appl. Catal. B Environ.* 226:360–372. <https://doi.org/10.1016/j.apcatb.2017.12.071>
- Dargahi Z, Asgharzadeh H, Maleki-Ghaleh H (2018) Synthesis of Mo-doped TiO₂/reduced graphene oxide nanocomposite for photoelectrocatalytic applications. *Ceram Int* 44(11):13015–13023. <https://doi.org/10.1016/j.ceramint.2018.04.120>
- Ambrožová N, Reli M, Šihor M, Kušrowski P, Wu JCS, Kočí K (2018) Copper and platinum doped titania for photocatalytic reduction of carbon dioxide. *Appl Surf Sci* 430:475–487. <https://doi.org/10.1016/j.apsusc.2017.06.307>
- Xie S, Wang Y, Zhang Q, Deng W, Wang Y (2014) MgO- and Pt-promoted TiO₂ as an efficient photocatalyst for the preferential reduction of carbon dioxide in the presence of water. *ACS Catal* 4(10):3644–3653. <https://doi.org/10.1021/cs500648p>
- Li X, Pan H, Li W, Zhuang Z (2012) Photocatalytic reduction of CO₂ to methane over HNb₃O₈ nanobelts. *Applied Catal A, Gen* 413–414(301):103–108. <https://doi.org/10.1016/j.apcata.2011.10.044>
- Sim LC, Leong KH, Saravanan P, Ibrahim S (2015) Rapid thermal reduced graphene oxide/Pt-TiO₂ nanotube arrays for enhanced visible-light-driven photocatalytic reduction of CO₂. *Appl Surf Sci* 358:122–129. <https://doi.org/10.1016/j.apsusc.2015.08.065>
- Tan LL, Ong WJ, Chai SP, Mohamed AR (2015) Noble metal modified reduced graphene oxide/TiO₂ ternary nanostructures for efficient visible-light-driven photoreduction of carbon dioxide into methane. *Appl Catal B Environ* 166–167:251–259. <https://doi.org/10.1016/j.apcatb.2014.11.035>
- Wang WN et al (2012) Size and structure matter: Enhanced CO₂ photoreduction efficiency by size-resolved ultrafine Pt nanoparticles on TiO₂ single crystals. *J Am Chem Soc* 134(27):11276–11281. <https://doi.org/10.1021/ja304075b>
- Kometani N, Hirata S, Chikada M (2017) Photocatalytic reduction of CO₂ by Pt-loaded TiO₂ in the mixture of sub- and supercritical water and CO₂. *J Supercrit Fluids* 120:443–447. <https://doi.org/10.1016/j.supflu.2016.05.031>
- Nabil S, Hammad AS, El-Bery HM, Shalaby EA, El-Shazly AH (2021) The CO₂ photoconversion over reduced graphene oxide based on Ag/TiO₂ photocatalyst in an advanced meso-scale continuous-flow photochemical reactor. *Environ Sci Pollut Res.* <https://doi.org/10.1007/s11356-021-13090-7>
- El-Bery HM, Matsushita Y, Abdel-moneim A (2017) Fabrication of efficient TiO₂-RGO heterojunction composites for hydrogen generation via water-splitting: comparison between RGO, Au and Pt reduction sites. *Appl Surf Sci* 423:185–196. <https://doi.org/10.1016/j.apsusc.2017.06.130>
- Yang X, Xiao T, Edwards PP (2011) The use of products from CO₂ photoreduction for improvement of hydrogen evolution in water splitting. *Int J Hydrogen Energy* 36(11):6546–6552. <https://doi.org/10.1016/j.ijhydene.2011.02.116>
- Chen W-Y, Shi G, Hailey AK, Tsai EST, Hammer N, Wu Z (2012) Photocatalytic conversion of carbon dioxide to organic compounds using a green photocatalyst: an undergraduate research experiment. *Chem Educ* 17(4):166–172. <https://doi.org/10.1007/s00897122438>
- Dong WH et al (2017) Coupling of photodegradation of RhB with photoreduction of CO₂ over rGO/SrTi_{0.95}Fe_{0.05}O_{3-Δ} catalyst: a strategy for one-pot conversion of organic pollutants to methanol and ethanol. *J Catal* 349:218–225. <https://doi.org/10.1016/j.jcat.2017.02.004>
- Nash T (1953) The colorimetric estimation of formaldehyde by means of the Hantzsch reaction. *Biochem J* 55(3):416–421. <https://doi.org/10.1042/bj0550416>
- Hong J, Zhang W, Ren J, Xu R (2013) Photocatalytic reduction of CO₂: a brief review on product analysis and systematic methods. *Anal Methods* 5(5):1086–1097. <https://doi.org/10.1039/c2ay26270c>
- Spurr RA, Myers H (1957) Quantitative analysis of anatase-rutile mixtures with an x-ray diffractometer. *Anal Chem* 29(5):760–762. <https://doi.org/10.1021/ac60125a006>
- Rajalakshmi K, Jeyalakshmi V, Krishnamurthy KR, Viswanathan B (2012) Photocatalytic reduction of carbon dioxide by water on titania: role of photophysical and structural properties. *Indian J. Chem. Sect A Inorg Phys. Theor. Anal. Chem.* 51:411–419
- Ola O, Maroto-Valer M, Liu D, MacKintosh S, Lee CW, Wu JCS (2012) Performance comparison of CO₂ conversion in slurry and monolith photoreactors using Pd and Rh-TiO₂ catalyst under ultraviolet irradiation. *Appl Catal B Environ* 126:172–179. <https://doi.org/10.1016/j.apcatb.2012.07.024>
- Jiang X et al (2018) Anatase and rutile in evonik aerioxide P25: Heterojunctioned or individual nanoparticles? *Catal. Today* 300(December):12–17. <https://doi.org/10.1016/j.cattod.2017.06.010>
- Tian B, Li C, Zhang J (2012) One-step preparation, characterization and visible-light photocatalytic activity of Cr-doped TiO₂ with anatase and rutile bicrystalline phases. *Chem Eng J* 191:402–409. <https://doi.org/10.1016/j.cej.2012.03.038>
- Bouras P, Stathatos E, Lianos P (2007) Pure versus metal-ion-doped nanocrystalline titania for photocatalysis. *Appl Catal B Environ* 73(1–2):51–59. <https://doi.org/10.1016/j.apcatb.2006.06.007>
- Liu L, Zhang Y, Zhang B, Feng Y (2017) A detailed investigation on the performance of dye-sensitized solar cells based on reduced graphene oxide-doped TiO₂ photoanode. *J Mater Sci* 52(13):8070–8083. <https://doi.org/10.1007/s10853-017-1014-9>
- Vasilaki E, Georgaki I, Vernardou D, Vamvakaki M, Katsarakis N (2015) Ag-loaded TiO₂/reduced graphene oxide nanocomposites for enhanced visible-light photocatalytic activity. *Appl Surf Sci* 353:865–872. <https://doi.org/10.1016/j.apsusc.2015.07.056>
- Dubey PK, Tripathi P, Tiwari RS, Sinha ASK, Srivastava ON (2014) Synthesis of reduced graphene oxide-TiO₂ nanoparticle composite systems and its application in hydrogen production. *Int J Hydrogen Energy* 39(29):16282–16292. <https://doi.org/10.1016/j.ijhydene.2014.03.104>

29. Melvin AA, Illath K, Das T, Raja T, Bhattacharyya S, Gopinath CS (2015) M-Au/TiO₂ (M = Ag, Pd, and Pt) nanophotocatalyst for overall solar water splitting: role of interfaces. *Nanoscale* 7(32):13477–13488. <https://doi.org/10.1039/c5nr03735b>
30. Wang P, Zhan S, Xia Y, Ma S, Zhou Q, Li Y (2017) The fundamental role and mechanism of reduced graphene oxide in rGO/Pt-TiO₂ nanocomposite for high-performance photocatalytic water splitting. *Appl Catal B Environ* 207:335–346. <https://doi.org/10.1016/j.apcatb.2017.02.031>
31. Hasan MR, Abd Hamid SB, Basirun WJ, Meriam Suhaimy SH, Che Mat AN (2015) A sol-gel derived, copper-doped, titanium dioxide-reduced graphene oxide nanocomposite electrode for the photoelectrocatalytic reduction of CO₂ to methanol and formic acid. *RSC Adv* 5(95):77803–77813. <https://doi.org/10.1039/c5ra12525a>
32. Mei BA, Munteshari O, Lau J, Dunn B, Pilon L (2018) Physical interpretations of nyquist plots for EDLC electrodes and devices. *J Phys Chem C* 122(1):194–206. <https://doi.org/10.1021/acs.jpcc.7b10582>
33. Tian H, Wan C, Zheng W, Hu X, Qiao L, Wang X (2016) Construction of a ternary hybrid of CdS nanoparticles loaded on mesoporous-TiO₂/RGO for the enhancement of photocatalytic activity. *RSC Adv* 6(88):84722–84729. <https://doi.org/10.1039/c6ra16094h>
34. Tasbihi M, Kočí K, Edelmannová M, Troppová I, Reli M, Schomäcker R (2018) Pt/TiO₂ photocatalysts deposited on commercial support for photocatalytic reduction of CO₂. *J Photochem Photobiol A Chem* 366:72–80. <https://doi.org/10.1016/j.jphotochem.2018.04.012>
35. Liu L, Li Y (2014) Understanding the reaction mechanism of photocatalytic reduction of CO₂ with H₂O on TiO₂-based photocatalysts: a review. *Aerosol Air Qual Res* 14(2):453–469. <https://doi.org/10.4209/aaqr.2013.06.0186>
36. Scalfani A, Herrmann JM (1996) Comparison of the photoelectronic and photocatalytic activities of various anatase and rutile forms of titania in pure liquid organic phases and in aqueous solutions. *J Phys Chem* 100(32):13655–13661. <https://doi.org/10.1021/jp9533584>
37. Li G et al (2008) Synthesizing mixed-phase TiO₂ nanocomposites using a hydrothermal method for photo-oxidation and photoreduction applications. *J Catal* 253(1):105–110. <https://doi.org/10.1016/j.jcat.2007.10.014>
38. Chang X, Wang T, Gong J (2016) CO₂ photo-reduction: insights into CO₂ activation and reaction on surfaces of photocatalysts. *Energy Environ Sci* 9(7):2177–2196. <https://doi.org/10.1039/c6ee00383d>
39. Shehzad N, Tahir M, Johari K, Murugesan T, Hussain M (2018) A critical review on TiO₂ based photocatalytic CO₂ reduction system: strategies to improve efficiency. *J CO₂ Util* 26:98–122. <https://doi.org/10.1016/j.jcou.2018.04.026>
40. Fox MA, Dulay MT (1993) Heterogeneous photocatalysis. *Chem Rev* 93(1):341–357. <https://doi.org/10.1016/B978-0-444-53178-0.00004-3>
41. Kočí K, Obalová L, Plachá D, Lacný Z (2008) Effect of temperature, pressure and volume of reacting phase on photocatalytic CO₂ reduction on suspended nanocrystalline TiO₂. *Collect Czechoslov Chem Commun* 73(8–9):1192–1204. <https://doi.org/10.1135/cccc20081192>
42. Cheng X et al (2017) An optofluidic planar microreactor for photocatalytic reduction of CO₂ in alkaline environment. *Energy* 120(41):276–282. <https://doi.org/10.1016/j.energy.2016.11.081>
43. Kalamaras E, Maroto-valer M, Xuan J, Wang H (2017) A Microfluidic reactor for solar fuel production from photocatalytic CO₂ reduction -the 15th international symposium on district heating and cooling photocatalytic CO₂ reduction. *Energy Procedia* 142:501–506. <https://doi.org/10.1016/j.egypro.2017.12.078>
44. Zhang QH, Han WD, Hong YJ, Yu JG (2009) Photocatalytic reduction of CO₂ with H₂O on Pt-loaded TiO₂ catalyst. *Catal Today* 148(3–4):335–340. <https://doi.org/10.1016/j.cattod.2009.07.081>

Publisher's Note Springer Nature remains neutral with regard to jurisdictional claims in published maps and institutional affiliations.

Authors and Affiliations

Samar Nabil¹  · Elsayed A. Shalaby¹ · Marwa F. Elkady^{2,3} · Yoshihisa Matsushita⁴ · Ahmed H. El-Shazly^{2,5}

✉ Samar Nabil
samar.nabil@alexu.edu.eg

¹ Department of Environmental Studies, Institute of Graduate Studies and Research, Alexandria University, Alexandria 21526, Egypt

² Chemical and Petrochemicals Engineering Department, Egypt-Japan University of Science and Technology, Alexandria 21934, Egypt

³ Fabrication Technology Department, Advanced Technology and New Materials Research Institute (ATNMRI), City of Scientific Research and Technological Applications, Alexandria, Egypt

⁴ Egypt-Japan University of Science and Technology, 179 New Borg El-Arab, Alexandria 21934, Egypt

⁵ Chemical Engineering Department, Faculty of Engineering, Alexandria University, Alexandria 21544, Egypt